Available online at www.sciencedirect.com
ScienceDirect
Computers and Structures 84 (2006) 1743–1759
Computers & Structures
www.elsevier.com/locate/compstruc

Modeling and estimation of the cardiac electromechanical activity

J. Sainte-Marie [a,b], D. Chapelle [a,*], R. Cimrman [c], M. Sorine [a]

[a] *INRIA-Rocquencourt, B.P. 105, 78153 Le Chesnay cedex, France*
[b] *CETMEF/LNHE, Chatou, France*
[c] *University of West Bohemia, Plzeň, Czech Republic*

Received 30 November 2005; accepted 19 May 2006
Available online 8 September 2006

Abstract

We describe an approach that we propose to model the electromechanical behavior of the heart, and to use the model in a data assimilation procedure in order to perform an identification of the parameters and state. The modeling of the heart tissue is based on an electrically activated contraction law formulated via multiscale considerations and is consistent with various physiological and thermomechanical key requirements. The global heart system also incorporates a simplified lumped modeling of the blood compartments. We report on numerical simulations and on validations of our model in reference and pathological conditions. Furthermore, the data assimilation procedure is intended to give access to quantities of interest for diagnosis purposes, and we present some promising results in this direction.

Keywords: Biomechanics; Heart modeling; Data assimilation; Computer-aided diagnosis

1. Introduction

The knowledge of the heart behavior and the power of data acquisition techniques (ECG, ultrasound or MRI images,...) have greatly improved during the last decades. In-vivo measurements of the cardiac activity are very valuable for clinical purposes, but some crucial biological quantities are hardly – or not at all – accessible, as for example stresses, pressures or constitutive parameters that may reflect pathologies. In order to reach these quantities *modeling* is required. On the other hand the complexity and diversity of the physical phenomena involved in the heart behavior are a major challenge for modeling. In particular the various data (constitutive parameters, boundary conditions, and so on) necessary to perform accurate simulations of the models cannot be determined *a priori*.

The work presented in this article has two objectives. The first is to model the (distributed) electromechanical behavior of the heart and to perform numerical simulations of the model, hence to obtain a physically based "cardiac simulator". After adequate calibration and validation of the model using clinical data, the simulator can be used in particular to represent some pathologies – e.g. an infarcted area as reflected in a dramatic decrease of local muscular excitability and contractility – and further to assess the impact of a given treatment (such as surgery or ventricular pacing) prior to implementation. Therefore an important perspective of this approach is to provide an assistance tool to medical decision-making.

The second objective is to "couple" the model with in-vivo measurements, i.e. to use the model in a data assimilation procedure in order to perform an identification of the parameters and state, hence to give access to quantities of interest for diagnosis purposes. Thus the challenge we pursue with this objective is to build a "computer-aided diagnosis" tool useful in a clinical environment.

The state of the art regarding the heart biomechanical modeling is already quite advanced and vast, see for example [22,10,20] and the references therein. In the approach

* Corresponding author. Tel.: +33 1 3963 5746; fax: +33 1 3963 5882.
E-mail address: dominique.chapelle@inria.fr (D. Chapelle).

0045-7949/$ - see front matter © 2006 Elsevier Ltd. All rights reserved.
doi:10.1016/j.compstruc.2006.05.003

proposed in this paper we – of course – do not intend to meet all the challenges and encompass the many aspects of the field. Nevertheless, the focus and originality of our work mainly lies in the following two ideas:

- We propose an active, electrically activated, large displacements and large strains model of cardiac tissue rigorously derived from physiological multiscale considerations and consistent with key thermomechanical requirements.
- The formulation and complexity of the proposed model is adjusted to the nature and amount of available measurements necessary for its calibration, with a view to data assimilation.

The outline of the paper is as follows. The forthcoming section presents the formulation of the complete (3D) excitation–contraction model. The next section is devoted to the description of discretization strategies. Section 4 then presents detailed simulation results of healthy and pathological behaviors. In Section 5 we describe our data assimilation approach and report on some preliminary results obtained with it. Finally we give some concluding remarks in Section 6.

2. The 3D heart model

In order to construct a model describing the three-dimensional (3D) electromechanical behavior of the heart, the following major ingredients are required:

- a constitutive law accounting for both the active and passive aspects in the behavior of the muscle fibres;
- a representation of the electrical activation – the input in the constitutive law – that can be obtained from modeling approaches of various types and complexities;
- a geometrical (or "anatomical") description of the myocardium incorporating the fibre directions;
- a model of the blood circulation inside and outside of the heart cavities, and also a model describing the opening and closure of the valves that separate the cavities from each other and from the external circulation.

We now discuss each of these items in details.

2.1. An excitation–contraction law for the myofibres

Most existing models of myofibre excitation–contraction mainly rely on heuristic approaches and experimental testing, whether directly at the macroscopic level [21], or in order to identify the attachment and detachment rates of the actin–myosin bridges in the sarcomeres [56].

By contrast, our approach follows the path opened by Huxley [23] – who has shown how actin–myosin bridge dynamics allows to describe the muscle contraction phenomena on the sarcomere scale – and Zahalak [57] – who used the method of moments with bridge dynamics in order to describe muscle contraction on the myofibre scale. Our model is based on a chemically controlled constitutive law of cardiac myofibre mechanics introduced in [5] and consistent with the behavior of myosin molecular motors [24]. The resulting sarcomere dynamics – derived by applying the moment-scaling method with the first two moments corresponding to active stiffness and stress, see [5] – is in agreement with the "sliding filament hypothesis" introduced in [23]. A particular choice of the attachment and detachment rates is made so that Hill's force–velocity relations for isotonic contraction become closure equations for the method of moments. This choice is a slight modification of that made in [23] or [57]: here these rates are not only dependent upon the sarcomere strain but also upon the strain rate. We recall this model briefly.

On a microscopic scale, the sarcomere is made up of thin and thick parallel filaments. When ATP (the fuel of the cell) is available and the level of intracellular calcium bound on troponin-C (the control of the contraction and relaxation in the sarcomeres) reaches a threshold ($Ca_{TnC} \geqslant \overline{C}$), the myosin heads of the thick filament that are not too far from actin sites on the thin filament ($\xi \in [0,1]$ for some microscopic strain), become likely to bind with the binding rate f.

Unbinding is due to the macroscopic strain rate $\dot{\varepsilon}_c$, or to the action of the calcium pumps under the threshold $\overline{C}$, or to large values of ξ. The unbinding rate is g. The previous conditions are translated into the following formulae (where $\mathbb{I}_S$ is the characteristic function of the set S) [5]:

$$f(\xi,t) = k_{\mathrm{ATP}} \cdot \mathbb{I}_{Ca_{TnC} \geqslant \overline{C}} \cdot \mathbb{I}_{\xi \in [0,1]},$$

$$g(\xi,t) = \alpha|\dot{\varepsilon}_c| + k_{\mathrm{SR}} \cdot \mathbb{I}_{Ca_{TnC} < \overline{C}} + k_{\mathrm{ATP}} \cdot \mathbb{I}_{Ca_{TnC} \geqslant \overline{C}} \cdot \mathbb{I}_{\xi \notin [0,1]}.$$

The parameter k_{ATP} represents the rate of the chemical reaction providing energy from the hydrolysis of ATP to the molecular motors in the sarcomere, whereas k_{SR} denotes the rate of bridge destruction due to sarcoplasmic reticulum pumps removing calcium ions from the troponin. The parameter α is dimensionless and positive.

It will be convenient to define a new control variable

$$u(t) = k_{\mathrm{ATP}} \cdot \mathbb{I}_{Ca_{TnC}(t) \geqslant \overline{C}} - k_{\mathrm{SR}} \cdot \mathbb{I}_{Ca_{TnC}(t) < \overline{C}}$$

so that $f(\xi,t) = |u(t)|_+ \cdot \mathbb{I}_{\xi \in [0,1]}$ and $f(\xi,t) + g(\xi,t) = \alpha|\dot{\varepsilon}_c| + |u(t)|$ where $|u|_+ = \max(0,u) = k_{\mathrm{ATP}} \cdot \mathbb{I}_{Ca_{TnC}(t) \geqslant \overline{C}}$ and $|u|_- = \max(0,-u) = k_{\mathrm{SR}} \cdot \mathbb{I}_{Ca_{TnC}(t) < \overline{C}}$ are ATP consumption rates during contraction and active relaxation respectively.

The interaction potential W^{am} of the actin–myosin system is responsible for muscle contraction corresponding to the negative values of the macroscopic strain ε_c describing the relative sliding of the actin over the myosin filament. Let $n(\xi,t)$ be the density of cross-bridges with strain ξ at time t. Then, Huxley's model is

$$\frac{\partial n}{\partial t} + \dot{\varepsilon}_c \frac{\partial n}{\partial \xi} = (1-n)f - ng,$$

$$\sigma_c(t) = -d(\varepsilon_c) \int_{-\infty}^{+\infty} \frac{\partial W^{\mathrm{am}}}{\partial \xi} n \, \mathrm{d}\xi + \mu_c \dot{\varepsilon}_c.$$

A parabolic W^{am} is chosen in [5]: $-\frac{\partial W^{\mathrm{am}}}{\partial \xi} = k_0\xi_0 + \sigma_0\xi$. The parameters k_0 and σ_0 are related to the number and

stiffness of available actin–myosin cross-bridges in the sarcomere, μ_c is a viscosity parameter and ξ_0 is a strain constant. The scaling technique to compute σ_c leads to introducing k_c and τ_c, respectively proportional to the zero and first-order moments of n:

$$k_c(t) = k_0 \int_{-\infty}^{+\infty} n(\xi, t)\,\mathrm{d}\xi \quad \text{and} \quad \tau_c(t) = \sigma_0 \int_{-\infty}^{+\infty} \xi n(\xi, t)\,\mathrm{d}\xi.$$

The resulting constitutive relation is given by the following system of ordinary differential equations:

$$\begin{cases} \dot{\tau}_c = k_c\dot{\varepsilon}_c - (\alpha|\dot{\varepsilon}_c| + |u|)\tau_c + \sigma_0|u|_+, & \tau_c(0) = \tau_{c_0}, \\ \dot{k}_c = -(\alpha|\dot{\varepsilon}_c| + |u|)k_c + k_0|u|_+, & k_c(0) = k_{c_0}, \\ \sigma_c = d(\varepsilon_c)(\tau_c + k_c\xi_0) + \mu_c\dot{\varepsilon}_c, \end{cases} \tag{1}$$

where u denotes the electrical input – corresponding to a normalized concentration of calcium bound on the troponin-C – with $u > 0$ during contraction and $u < 0$ during active relaxation. The modeling of u is further elaborated in Section 2.2 and the meaning of $d(\varepsilon_c)$ is discussed in the next section.

2.1.1. Starling effect

The Starling effect is one of the most important regulatory mechanisms of the heart activity. By this mechanism, when the preload increases the heart is able to also increase its contraction. The preload corresponds to the stretching of the cardiac fibres at the end of the previous diastolic filling, hence it is related to the veinous return and the pressure in the atria. Thus, increasing the ventricular end-diastolic pressure leads to an increased stroke volume, see Fig. 1. The Starling effect can also be interpreted by saying that the heart adapts its contraction so that the stroke volume compensates the end-diastolic volume.

The underlying physiological mechanism is as follows. When the stretching of the sarcomere increases, the troponin-C calcium sensitivity also increases leading to a growth of the cross-bridge attachment availability. This means that when the stretching of the sarcomere increases we move from point (a) to (b) on the curve presented in Fig. 2(i), in which I denotes the normal range for the sarcomere length. This phenomenon is no more valid for very large stretching of the sarcomere, as represented by (c) in the figure. These various states of deformation are also schematically depicted in Fig. 3. It appears that for large deformations fewer actin–myosin cross-bridges can be created. This leads to the factor $d(\varepsilon_c)$ introduced in [38]. This factor is a function with values in the interval $[0, 1]$ and behaving as represented in Fig. 2(ii).

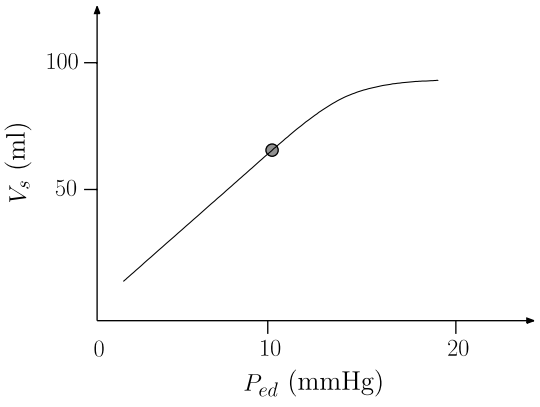

Fig. 1. The Franck–Starling curve (V_s: stroke volume, P_{ed}: left ventricular end-diastolic pressure).

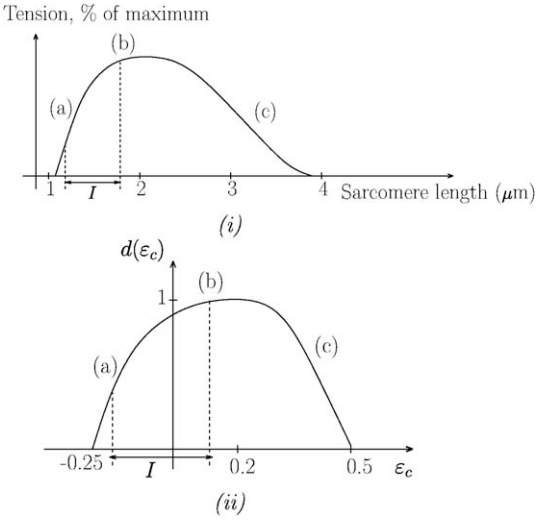

Fig. 2. (i) The "length-tension" curve of a muscle with the three different configurations of the sarcomere shown in Fig. 3 and (ii) the corresponding modulation $d(\varepsilon_c)$ of the active stress σ_c.

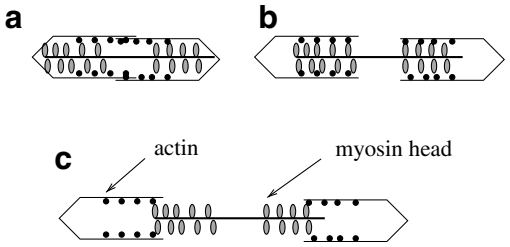

Fig. 3. Three different sarcomere deformations.

2.1.2. Thermomechanical compatibility

The stress in the myofibre is σ_c as given in System (1). Taking $0 \leqslant k_c(0) \leqslant k_0$, Eq. (1)-b ensures that $0 \leqslant k_c \leqslant k_0$ at all times. In fact, k_c can be seen as the progress of the chemical reactions governing the creation (resp. destruction) of cross-bridges via the calcium/troponin-C binding (resp. ATP hydrolysis). For small values of k_c, few cross-bridges are fastened whereas for $k_c \approx k_0$ the majority of the actin–myosin bridges are attached.

Let us introduce the quantity r defined by

$$r = |u| + \alpha|\dot{\varepsilon}_c|,$$

homogeneous to a time rate. Then the first equation of (1) can be rewritten in the form

$$\dot{\tau}_c = r\left(\frac{k_c\dot{\varepsilon}_c + \sigma_0|u|_+}{r} - \tau_c\right). \tag{2}$$

Assuming that $\dot{\varepsilon}_c$ is bounded ($|\dot{\varepsilon}_c| \leqslant a$), we can show that σ_c is also bounded by using (2) to obtain

$$\begin{aligned}|\tau_c| &\leqslant \max\left\{\sup_t \frac{|k_c\dot{\varepsilon}_c + \sigma_0|u|_+|}{\alpha|\dot{\varepsilon}_c| + |u|}, |\tau_c(0)|\right\}\\ &\leqslant \max\left\{\sigma_0 + \frac{k_0}{\alpha}, |\tau_c(0)|\right\}.\end{aligned}$$

Taking in particular $|\tau_c(0)| \leqslant \sigma_0 + k_0/\alpha$ we see that $|\tau_c| \leqslant \sigma_0 + k_0/\alpha$ always holds.

We can further interpret the active constitutive law by considering $\tilde{\tau}_c = \tau_c + k_c\xi_0$, and rewriting System (1) as

$$\begin{cases}\dot{\tilde{\tau}}_c = k_c\dot{\varepsilon}_c - (\alpha|\dot{\varepsilon}_c| + |u|)\tilde{\tau}_c + (\sigma_0 + k_0\xi_0)|u|_+, & \tilde{\tau}_c(0) = \tau_{c_0} + k_{c_0}\xi_0,\\ \dot{k}_c = -(\alpha|\dot{\varepsilon}_c| + |u|)k_c + k_0|u|_+, & k_c(0) = k_{c_0},\\ \sigma_c = d(\varepsilon_c)\tilde{\tau}_c + \mu_c\dot{\varepsilon}_c.\end{cases}$$

This shows that an appropriate redefinition of σ_0 allows to consider $\xi_0 = 0$ in (1), which we henceforth do consider. Introducing ε_c^e defined by $\tau_c = k_c\varepsilon_c^e$ – note that ε_c^e can be seen as the elastic part of ε_c – and substituting in the first equation of (1) we obtain

$$\dot{\varepsilon}_c^e = \dot{\varepsilon}_c + \frac{\sigma_0}{k_c}|u|_+ - \frac{k_0}{k_c}|u|_+\varepsilon_c^e. \tag{3}$$

Now, defining $\varepsilon_c = \varepsilon_c^e + \varepsilon_c^p$ we have

$$\dot{\varepsilon}_c^p = -\frac{\sigma_0}{k_c}|u|_+ + \frac{k_0}{k_c}|u|_+\varepsilon_c^e. \tag{4}$$

Consider first the case $d(\varepsilon_c) = 1$. The internal mechanical power corresponding to the constitutive law (1) is given by

$$\begin{aligned}\sigma_c\dot{\varepsilon}_c &= \frac{\partial\left(\frac{k_c}{2}(\varepsilon_c^e)^2\right)}{\partial t} + \mu_c\dot{\varepsilon}_c^2 + k_c\varepsilon_c^e\dot{\varepsilon}_c^p - \dot{k}_c\frac{(\varepsilon_c^e)^2}{2}\\ &= \frac{\partial\left(\frac{k_c}{2}(\varepsilon_c^e)^2\right)}{\partial t} + \mu_c\dot{\varepsilon}_c^2 + k_c\varepsilon_c^e\dot{\varepsilon}_c^p\\ &\quad + \frac{(\varepsilon_c^e)^2}{2}((\alpha|\dot{\varepsilon}_c| + |u|)k_c - k_0|u|_+).\end{aligned}$$

By (4) we have

$$k_c\varepsilon_c^e\dot{\varepsilon}_c^p = k_0|u|_+(\varepsilon_c^e)^2 - \sigma_0|u|_+\varepsilon_c^e,$$

hence the following expression holds for the mechanical power:

$$\begin{aligned}\sigma_c\dot{\varepsilon}_c &= \frac{\partial\left(\frac{k_c}{2}(\varepsilon_c^e)^2\right)}{\partial t} + \mu_c\dot{\varepsilon}_c^2 + \frac{(\varepsilon_c^e)^2}{2}(k_0|u|_+ + (\alpha|\dot{\varepsilon}_c| + |u|)k_c)\\ &\quad - \sigma_0|u|_+\varepsilon_c^e.\end{aligned} \tag{5}$$

We have the following thermomechanical interpretation: $\frac{1}{2}k_c(\varepsilon_c^e)^2$ appears as a free energy, whereas $\mu_c\dot{\varepsilon}_c^2 + \alpha|\dot{\varepsilon}_c|k_c\frac{(\varepsilon_c^e)^2}{2}$ is a non-negative pseudo-potential of dissipation. Therefore the second principle of thermodynamics is satisfied. Furthermore the terms $(k_0|u|_+ + |u|k_c)\frac{(\varepsilon_c^e)^2}{2} - \sigma_0|u|_+\varepsilon_c^e$ represent "exogenous energy" due to the electrical input. More precisely, since $\varepsilon_c^e = \frac{\tau_c}{k_c}$ we can rewrite (5) as

$$\begin{aligned}\sigma_c\dot{\varepsilon}_c - \frac{\partial\left(\frac{k_c}{2}(\varepsilon_c^e)^2\right)}{\partial t} &= \mu_c\dot{\varepsilon}_c^2 + \frac{(\tau_c)^2}{2k_c}(\alpha|\dot{\varepsilon}_c| + |u|)\\ &\quad + \left(\frac{k_0}{2}\frac{\tau_c^2}{k_c^2} - \sigma_0\frac{\tau_c}{k_c}\right)|u|_+,\end{aligned} \tag{6}$$

where it appears that some energy can be supplied to the system only when $u > 0$ and $0 < \tau_c \leqslant 2\sigma_0\frac{k_c}{k_0 + k_c}$.

Taking into account the Starling effect, (6) becomes

$$\begin{aligned}\sigma_c\dot{\varepsilon}_c - \frac{\partial\left(d(\varepsilon_c)\frac{k_c}{2}(\varepsilon_c^e)^2\right)}{\partial t} &= \mu_c\dot{\varepsilon}_c^2 + \frac{d(\varepsilon_c)(\tau_c)^2}{2k_c}(\alpha|\dot{\varepsilon}_c| + |u|)\\ &\quad + d(\varepsilon_c)\left(\frac{k_0}{2}\frac{\tau_c^2}{k_c^2} - \sigma_0\frac{\tau_c}{k_c}\right)|u|_+\\ &\quad - \dot{\varepsilon}_c d'(\varepsilon_c)\frac{\tau_c^2}{2k_c},\end{aligned} \tag{7}$$

where in order to satisfy the second principle of thermodynamics $d(\varepsilon_c)$ is chosen so that $\alpha d \geqslant |d'|$. In the sequel the variations of $d(\varepsilon_c)$ correspond to those depicted in Fig. 2(ii).

2.2. Electrical activation

The propagation of the action potential v in the cardiac tissue results from the diffusion of calcium, sodium and potassium ions in the extracellular space, from ionic currents through the cell membrane and from reactions of these ions in the intracellular space. There are many different types of ionic channels (and corresponding current models), some of them having an open/closed state modeled by gate variables. Let I_{ion} be the total equivalent electrical current through the membrane. In the intracellular space the reactions involve the concentrations of calcium bound on various proteins, in particular troponin-C that regulates Ca^{2+} induced muscle contraction, as already mentioned. Let w be the vector of all concentrations and ionic gating variables involved in the intracellular reactions and ionic channels. Then the general monodomain models for v is a reaction–diffusion equation for v coupled with an ODE for w (see e.g. [29] and references therein), as represented in the following system where I_{ext} denotes a stimulation current, c_m, $\underline{\sigma}_m$ are some (scalar) capacitance and (tensor) conductivity:

$$\begin{cases}c_m\frac{\partial v}{\partial t} - \operatorname{div}(\underline{\sigma}_m.\underline{\nabla}v) + I_{\text{ion}}(v,w) = I_{\text{ext}} & \text{in } \Omega_H,\\ \frac{\partial w}{\partial t} - R(v,w) = 0 & \text{in } \Omega_H,\\ \underline{\nu}.(\underline{\sigma}_m\underline{\nabla}v) = 0 & \text{on } \partial\Omega_H,\end{cases} \tag{8}$$

where Ω_H denotes the heart tissue domain and $\partial\Omega_H$ its boundary with unit outward normal vector $\underline{\nu}$. Remark that in bidomain models an external potential and an external conductivity are also considered, leading to a slight modification of (8), see [29,42].

In our simulations we have used a very simple monodomain model, a variant of the two-variable FitzHugh–Nagumo model proposed by Aliev and Panfilov [1], where w is a scalar "repolarization potential", viz.

$$\begin{cases} c_m^{-1} I_{\text{ion}}(v,w) = kv(v-a)(v-1) + vw, \\ R(v,w) = \varepsilon(v,w)(-w - kv(v-a-1)), \end{cases} \tag{9}$$

with $\varepsilon(v,w) = \varepsilon_0 + \mu_1 w/(v+\mu_2)$ and k, a, ε_0, μ_1, μ_2 positive parameters. This model is able to generate v-traveling waves sufficiently realistic for our purpose, i.e. simulating isolated heart beats in various conditions. For a series of heart beats it would be necessary to consider a more realistic calcium dynamics than the simple w-repolarization dynamics. Nevertheless, we need an output variable similar to Ca_{TnC}, an output available only in models with higher dimensional w, as e.g. in [13]. Note that, given a realistic v-traveling wave – e.g., generated by (9) – it is possible to use it as the input of a more complete ODE of the form $\frac{\partial w}{\partial t} - R(v,w) = 0$ to generate a w-traveling wave and then to estimate the desired output. Remark also a drawback of this heuristic approach: it is difficult to take into account possible mechano-electric feedback loops, as e.g. the dependence of the rate of Ca-detachment from troponin-C upon the sarcomere tension (or stretch rate) [19], which we do not consider here. In fact, in our heart model we have used (9) with a simple affine relation between u and v: $u = h(v - \bar{v})$. This approach is substantiated by the similitude of the v and Ca_{TnC} waveforms obtained with the more refined model of [13], as shown in Fig. 4.

Finally, we have considered several types of activation models:

- A uniform activation without propagation, $u(M,t) \equiv u(t)$ for all points M of the muscle.
- A simplified propagation mechanism with $u(M,t) = h(v^*(t - \Pi M/c) - \bar{v})$ where v^* is an action potential template, ΠM is the projection of M along the apex to the base axis and c is the velocity of the wavefront.
- A traveling wave generated with a reaction–diffusion model as described above.

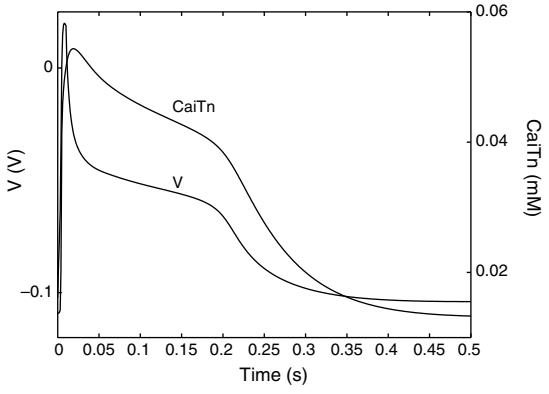

Fig. 4. Responses of the action potential v and concentration of calcium buffered on troponin-C (Ca_{TnC}) for an external stimulation current I_{ext} modeled as an impulse at time 0 (taken from [13]).

2.3. 3D mechanical modeling of the cardiac tissue

In this section, we describe how the electrically activated contraction law presented above is used in a 3D continuum mechanics framework formulated for large displacements and strains – as is observed in the actual behavior of the heart.

2.3.1. Definitions and notations

The definitions and notations used for the description of the mechanical model are the following:

- $\underline{y}$ denotes the displacement field,
- $\underline{\underline{F}}$ the deformation gradient, namely, $\underline{\underline{F}} = \underline{\underline{1}} + \underline{\nabla y}$,
- $\underline{\underline{C}}$ the right Cauchy–Green deformation tensor, viz. $\underline{\underline{C}} = \underline{\underline{F}}^{\mathrm{T}} \cdot \underline{\underline{F}}$,
- $\underline{\underline{E}}$ the Green–Lagrange strain tensor, i.e. $\underline{\underline{E}} = \frac{1}{2}(\underline{\underline{C}} - \underline{\underline{1}})$,
- $\underline{\underline{\Sigma}}$ the second Piola–Kirchhoff stress tensor, namely, the stress tensor which is energy-conjugate to $\underline{\underline{E}}$.

We recall that the three classical strain invariants are defined by

$$I_1 = \mathrm{Tr}\,\underline{\underline{C}}, \quad I_2 = \frac{1}{2}((\mathrm{Tr}\,\underline{\underline{C}})^2 - \mathrm{Tr}\,\underline{\underline{C}}^2), \quad I_3 = \det \underline{\underline{C}}.$$

We will also use the so-called reduced invariants given by

$$\tilde{I}_1 = I_1 J^{-\frac{1}{3}}, \quad \tilde{I}_2 = I_2 J^{-\frac{2}{3}}, \quad J = (I_3)^{\frac{1}{2}}.$$

2.3.2. The rheological model

The myofibre constitutive law described above is now incorporated in a rheological model of Hill-Maxwell type [7,16,46], as depicted in Fig. 5a. The element E_c accounts for the contractile electrically activated behavior governed by (1) and all symbols appearing with index c refer to this element. An elastic material law is used for the series element E_s and a visco-elastic behavior is considered for the parallel branch E_p. The stress–strain law for E_s – which plays an important role during isovolumetric phases – is generally assumed to be linear [37], and we follow this assumption in our modeling. The role of E_p, described in details in Section 2.3.3, is – in particular – to prevent the heart from overstepping certain limits during filling or ejection.

In the active branch the only relevant deformations are those occurring along the direction of the muscle fibres, namely 1D deformations. Denoting by $\underline{n}$ the unit-length vector that represents the fibre direction at any point in the reference configuration, we thus define

$$\varepsilon_{1\mathrm{D}} = \sum_{i,j} E_{ij} n_i n_j. \tag{10}$$

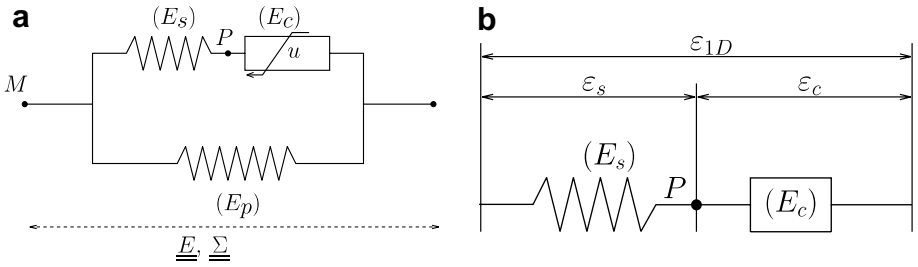

Fig. 5. (a) Hill-Maxwell rheological model and (b) strains in the active branch.

Because of large deformations, the individual deformations within the active branch (depicted in Fig. 5b) compose according to a multiplicative – not additive – rule, viz.

$$1 + 2\varepsilon_{1D} = (1 + 2\varepsilon_c)(1 + 2\varepsilon_s), \tag{11}$$

and thermodynamical considerations entail that the resulting generated tension is [32]

$$\sigma_{1D} = \frac{\sigma_c}{1 + 2\varepsilon_s} = \frac{\sigma_s}{1 + 2\varepsilon_c}. \tag{12}$$

2.3.3. Description of the parallel branch

We now focus on the description of the parallel element E_p. Considering an isothermal process, the satisfaction of the Clausius–Duhem inequality [53] in the absence of dissipation leads to

$$\underline{\underline{\Sigma}}_p = \rho_0 \frac{\partial W^e}{\partial \underline{\underline{E}}},$$

ρ_0 being the density expressed in the reference state and W^e a hyperelastic strain energy potential. When viscosity is considered, the Clausius–Duhem inequality becomes

$$\left(\underline{\underline{\Sigma}}_p - \rho_0 \frac{\partial W^e}{\partial \underline{\underline{E}}}\right) : \dot{\underline{\underline{E}}} \geqslant 0, \quad \forall \underline{\underline{E}}, \dot{\underline{\underline{E}}},$$

and a viscous pseudo-potential $W^v(\underline{\underline{E}}, \dot{\underline{\underline{E}}})$ accounting for energy dissipation ought to satisfy

$$\frac{\partial W^v}{\partial \dot{\underline{\underline{E}}}} : \dot{\underline{\underline{E}}} \geqslant 0, \quad \forall \dot{\underline{\underline{E}}}. \tag{13}$$

This holds – in particular – when W^v is a convex function of $\dot{\underline{\underline{E}}}$ with $\frac{\partial W^v}{\partial \dot{\underline{\underline{E}}}}(\underline{\underline{0}}) = \underline{\underline{0}}$, which are natural assumptions.

Taking dissipation into account we thus have

$$\underline{\underline{\Sigma}}_p(\underline{\underline{E}}, \dot{\underline{\underline{E}}}) = \rho_0 \frac{\partial W^e}{\partial \underline{\underline{E}}} + \frac{\partial W^v}{\partial \dot{\underline{\underline{E}}}} = \underline{\underline{\Sigma}}^e_p(\underline{\underline{E}}) + \underline{\underline{\Sigma}}^v_p(\underline{\underline{E}}, \dot{\underline{\underline{E}}}).$$

Two families of material laws are frequently used in the literature for the modeling of soft tissues, namely, Mooney–Rivlin materials and Veronda–Westmann materials [15,18,28,54]. In this context W^e appears as a linear combination of the following terms

$$\begin{aligned} W^e_1 &= \kappa_1(\tilde{I}_1 - 3) \quad \text{neo–Hookean term,} \\ W^e_2 &= \kappa_2(\tilde{I}_2 - 3) \quad \text{Mooney–Rivlin term,} \\ W^e_3 &= \kappa_3(e^{\eta(\tilde{I}_1 - 3)} - 1) \quad \text{Veronda–Westmann term.} \end{aligned} \tag{14}$$

We point out that several authors do not restrict the choice of elastic constitutive law to hyperelastic materials and focus on fitting stress–strain curves with experimental data. The most widely used experimental-based stress–strain law is called the "pole-zero law" and has been introduced by Hunter [50,39], see also [33] for an alternative approach. This remark also prevails for the design of the active constitutive law describing the muscle fibres, see [56].

In our simulations we have considered a Mooney–Rivlin material, namely,

$$W^e = \kappa_1(\tilde{I}_1 - 3) + \kappa_2(\tilde{I}_2 - 3).$$

Regarding the viscous part of the behavior, we used

$$W^v = \frac{\eta}{2} \dot{\underline{\underline{E}}} : \dot{\underline{\underline{E}}},$$

see also Pioletti et al. [45] for a more complex viscous pseudo-potential function.

The calibration of the parameters appearing in W^e and W^v will be discussed in Section 4.1.

2.3.4. 3D constitutive equations and equilibrium

In the model, we do not consider exact incompressibility and instead the volume variations of the muscle are penalized. The rheological model described above leads to

$$\underline{\underline{\Sigma}} = -pJ\underline{\underline{C}}^{-1} + \underline{\underline{\Sigma}}^e_p(\underline{\underline{E}}) + \underline{\underline{\Sigma}}^v_p(\underline{\underline{E}}, \dot{\underline{\underline{E}}}) + \sigma_{1D}\underline{n} \otimes \underline{n}, \tag{15}$$

where the symbol $\otimes$ denotes tensorial product, hence the term $\sigma_{1D}\underline{n} \otimes \underline{n}$ expresses that active stresses arise along the fibre directions. The first term in Eq. (15) corresponds to the volumetric behavior described by

$$W^{vol} = K(J - 1) - K \ln J, \quad \frac{\partial W^{vol}}{\partial \underline{\underline{E}}} = -pJ\underline{\underline{C}}^{-1},$$

with $p = K\left(\frac{1-J}{J}\right)$, K being a large bulk modulus ensuring an approximate incompressibility of the cardiac tissue, see [32]. Note that, when the coronary microcirculation is considered – which is not the case here – changes of volumes must instead be related to internal fluid flows.

In addition, in Eq. (15) the quantities $\underline{\underline{\Sigma}}^e_p(\underline{\underline{E}})$ and $\underline{\underline{\Sigma}}^v_p(\underline{\underline{E}}, \dot{\underline{\underline{E}}})$ represent the elastic and viscous parts – respectively – in the parallel branch as described above.

Finally, the material behavior is completely described by (15), where

- σ_{1D} can be expressed as a function of $\underline{\underline{E}}$ (through ε_{1D}, see (10)) and ε_c using Eqs. (11), (12), and the series element elastic law, namely,

$$\sigma_{1D} = \frac{\sigma_s}{1+2\varepsilon_c} = \frac{E_s[(\varepsilon_{1D}-\varepsilon_c)/(1+2\varepsilon_c)]}{1+2\varepsilon_c}, \tag{16}$$

- $\underline{\underline{E}}$ and ε_c are related by the equilibrium equation in the series branch, viz.

$$\sigma_c \frac{1+2\varepsilon_c}{1+2\varepsilon_{1D}} = \frac{E_s[(\varepsilon_{1D}-\varepsilon_c)/(1+2\varepsilon_c)]}{1+2\varepsilon_c}, \tag{17}$$

- σ_c being related to ε_c through the dynamical system (1) (where we recall that u is seen as an input).

2.4. Coupling with the blood compartments

Considering the complexity of the heart muscle behavior alone, modeling the complete fluid–structure interaction phenomena relative to internal fluid flows is largely out of reach, particularly with a view to estimation – namely solving inverse problems. Therefore we approximate the blood inside each ventricle by a simplified system described by a global volume and a uniform pressure.

The successive phases of the cardiac cycle are distinguished in the coupling conditions between the various blood compartments – inside the ventricles and in the other parts of the cardiovascular system. With P_v denoting the blood pressure inside a ventricle, P_{ar} the pressure in the corresponding artery outlet and P_{at} the pressure in the corresponding atrium, ejection occurs when $P_v \geqslant P_{ar}$ whereas the valve between ventricle and atrium opens when $P_v \leqslant P_{at}$, see Fig. 6a.

2.4.1. The phases of the cardiac cycle

The cardiac cycle can be decomposed into four successive phases: isovolumetric contraction; ejection; isovolumetric relaxation; filling. The first two phases constitute the *systole*; the last two phases make up the *diastole*. From a mechanical point of view, the formulations of the complete problem arising during the isovolumetric phases – namely, with closed valves – and the non-isovolumetric phases are quite different as to how the pressure and volume of the blood in the ventricles are governed. Denoting by $V^{(t)}$ the volume of the ventricle cavity at a given time t, during isovolumetric phases we have $\dot{V}^{(t)} = 0$ – namely, a constraint to be enforced on the tissue displacements – and the internal pressure P_v corresponds to the Lagrange multiplier associated with this constraint. By contrast, during non-isovolumetric phases (ejection and filling) we have $P_v = P_{ext}$ where P_{ext} equals P_{ar} or P_{at} according to which external compartment communicates with the ventricle. Moreover, during all phases the internal pressure gives a natural boundary condition in the form

$$J^{-1}(\underline{\underline{F}} \cdot \underline{\underline{\Sigma}} \cdot \underline{\underline{F}}^{T}) \cdot \underline{v}^{(t)} = -P_v \underline{v}^{(t)}, \tag{18}$$

on the part of the (deformed) boundary corresponding to the endocardium, $\underline{v}^{(t)}$ denoting the unit-length normal vector pointing outward with respect to the tissue.

2.4.2. Valve opening and closure

In our simplified view of the blood compartments we model the opening and closure of the valves by relations similar to those arising in the Signorini contact problem. For a more detailed modeling of the valve mechanics, see in particular [43]. Namely, considering the blood flow leaving a ventricle $q = -\dot{V}$ we write

$$\begin{cases} q \leqslant 0 & \text{when } P_v = P_{at} \quad \text{(filling)}, \\ q = 0 & \text{when } P_{at} < P_v < P_{ar} \quad \text{(isovol. phases)}, \\ q \geqslant 0 & \text{when } P_v = P_{ar} \quad \text{(ejection)}. \end{cases} \tag{19}$$

However, relation (19) is not regular, hence it is not practical from a computational point of view and a regularized version is needed (see Fig. 6b). We thus instead use

$$\begin{cases} q = K_{at}(P_v - P_{at}) & \text{when } P_v \leqslant P_{at}, \\ q = K_p(P_v - P_{at}) & \text{when } P_{at} \leqslant P_v \leqslant P_{ar}, \\ q = K_{ar}(P_v - P_{ar}) + K_p(P_{ar} - P_{at}) & \text{when } P_v \geqslant P_{ar}, \end{cases} \tag{20}$$

which is depicted by the solid curve in Fig. 6b. This system defines

$$q = f(P_v, P_{ar}, P_{at}), \tag{21}$$

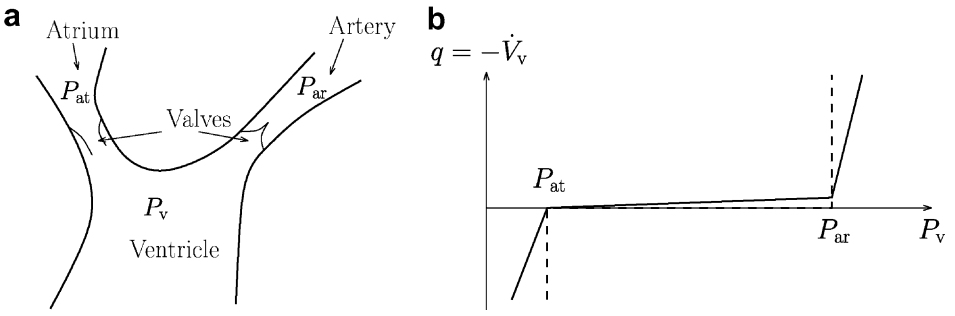

Fig. 6. Aortic and mitral valves model, (a) mechanism and (b) formulation as a double contact problem, (--) relation (19) and (–) relation (20).

namely, the blood flow as a regular function of the pressures in the three compartments. During ejection and filling (20) corresponds to linear laws where the coefficients are related to the radius of the valves, see [35]. During the isovolumetric phases, the constraint "$q = 0$" is relaxed using relation $q = K_{\mathrm{p}}(P_{\mathrm{v}} - P_{\mathrm{at}})$ with K_{p} much smaller than K_{ar} and K_{at}, which can be interpreted as a penalization strategy.

2.4.3. Windkessel models

In order to obtain an accurate response of the model during non-isovolumetric phases – and particularly during ejection – we also need to model the external blood circulation, which accounts for the variations of P_{ar} along the cardiac cycle. An extensive literature exists on the formulation and calibration of arterial pressure-flow relations in the form of time-dependent ODEs, often called "Windkessel models". We have also experimented with 1D arterial models – namely, with one space variable in addition to time – of the type described in [14], but the scarcity of calibration data and results makes such models presently inadapted to estimation purposes and we do not further report on the corresponding simulations in this paper.

Windkessel and similar lumped models are often used to represent blood flow and pressure in arteries. These models can be derived from electrical circuit analogies where current and voltage represent arterial flow and pressure, respectively. The original ideas for such models were first proposed by S. Hales in 1733 and further developed by O. Frank in 1899. For more detailed information and references on Windkessel models, we refer to e.g. [2,38,51,55].

In our simulations, we used the three-element Windkessel model depicted in Fig. 7. The corresponding pressure-flow relation reads

$$C\dot{P}_{\mathrm{ar}} + \frac{P_{\mathrm{ar}} - P_{\mathrm{ve}}}{R_p} = \left(1 + \frac{R_c}{R_p}\right) q + R_c C \dot{q}, \tag{22}$$

where P_{ve} denotes the venous pressure. This relation is only valid during ejection, namely when $q > 0$. During isovolumetric phases and ventricular filling, arterial pressure is instead described by

$$C\dot{P}_{\mathrm{ar}} + \frac{P_{\mathrm{ar}} - P_{\mathrm{ve}}}{R_p} = 0. \tag{23}$$

Note that we use two such models to represent both the systemic and pulmonary circulations. This three-element Windkessel model has been found to be in excellent agreement – after proper adjustment of the resistance and capacitance parameters – with clinical measurements, see [51]. In Fig. 7 the arrows for C and R_p indicate that these quantities can also be varied to account for nervous system regulation.

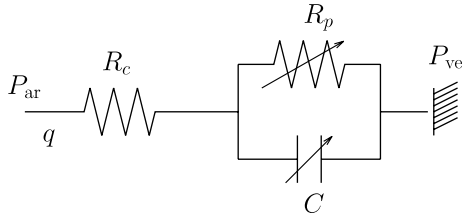

Fig. 7. The three-element Windkessel model.

2.4.4. Modeling of the atria

Unlike for the ventricles, we do not consider a continuum mechanics model of the atria and instead account for atrial compartments by assuming that they create a (prescribed) low blood pressure allowing ventricular filling during diastole. The prescribed value of atrial pressure is increased before ventricular systole to represent atrial contraction. Note that – in order to obtain a more complex behavior – the modeling of atrial contraction could be performed using a 0D model (namely, a time-dependent ODE).

2.5. Boundary conditions

The boundary conditions used for the structure take into account the following two phenomena:

- the base of the myocardium is fastened to the arteries and the veins;
- the apex of the myocardium is almost still along a cardiac cycle whereas the base moves.

The previous requirements are satisfied using springs and dashpots located at the base, see Fig. 8, and a translation is applied on the computed displacements to obtain a still apex.

Let us consider a point A belonging to the curve Δ (solid part) of Fig. 8, if $\underline{A}^{(t)}$ denotes the position of A at time t then the force acting on A is

$$\underline{F}^{A} = k(\underline{A}^{(0)} - \underline{A}^{(t)}) - c\dot{\underline{A}}^{(t)}.$$

The velocity term $\dot{\underline{A}}^{(t)}$ is discretized as $\dot{\underline{A}}^{(t)} \approx \frac{1}{\Delta t}(\underline{A}^{(t)} - \underline{A}^{(t-1)})$.

However, it is necessary to allow the base to undergo significant displacements in the transverse $(\vec{x}, \vec{y})$ directions, in particular during ejection and filling. Hence, for a point B belonging to the dashed part of Δ we prescribe the force

$$\underline{F}^{B} = k\Pi_z(\underline{B}^{(0)} - \underline{B}^{(t)}) - c\Pi_z\dot{\underline{B}}^{(t)},$$

Π_z being the projection on the $\vec{z}$ axis.

2.6. Initial conditions

Adequate initial conditions need be prescribed, although in practice they are very difficult to estimate. We considered an initial time t_0 corresponding to the end of the filling i.e. $q = -\dot{V} = 0$ and $u \equiv 0$, and we prescribed "realistic" initial values for the displacements $y(M, t_0) = y_0(M)$, the contractile strains, stiffnesses and stresses (namely, $\varepsilon_c(M, t_0) = \varepsilon_{c,0}(M)$, $k_c(M, t_0) = k_{c,0}(M)$ and $\tau_c(M, t_0) = \tau_{c,0}(M)$, respectively). Since the system is supposed to have reached a static equilibrium, we also have $P_{\mathrm{v}}(t_0) = P_{\mathrm{at}}(t_0)$.

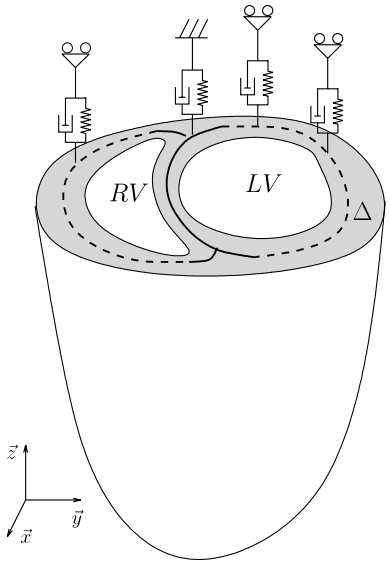

Fig. 8. Springs and dashpots fastening the myocardium.

Nevertheless, it is to be noted that the system is meant to behave in a periodic manner, and in fact rapidly reaches an attractor (limit cycle), whether after initialization or modification of the parameters, see Section 4. Hence, since the initial conditions are "forgotten" by the system after a few cycles, their precise specification is not a crucial issue.

2.7. Geometrical model

We generated a "generic" anatomical model of the myocardium with a simple geometry. In a first step we use truncated ellipsoids to define a simplified geometry of the epicardium and endocardium, with fibre orientations featuring an elevation angle varying linearly from $+90°$ to $-90°$ across the wall. We point out that this is consistent with experimental data as provided by diffusion tensor imaging and dissection analysis [17,36]. Then, this simplified geometry is modified by an adjustment procedure to closely fit the segmented geometry of a heart acquired using MRI, see [48] for details on this procedure. The resulting mesh considered in our simulations is shown in Fig. 9, with the fibre orientations displayed in Fig. 10.

As seen in Fig. 9, the anatomical data considered correspond to a truncation of the heart below the valve rings. We then defined the ventricular internal volumes using contour lines of the endocardium in each ventricle near the truncation and the barycenters of the contour lines in order to construct the surfaces needed to close the volumes, see Fig. 11. Hence each ventricular volume considered corresponds to the volume enclosed within the endocardium $\Gamma_E^{(t)}$ and this additional surface $\Gamma_O^{(t)}$.

2.8. Principle of virtual work and summary of governing equations

We use a total Lagrangian formulation and denote by Ω_H the reference domain corresponding to cardiac tissue, while the part of the boundary corresponding to ventricular endocardium is denoted by $\Gamma_{El} \cup \Gamma_{Er}$ (referring to the left and right ventricles). The principle of virtual work then gives

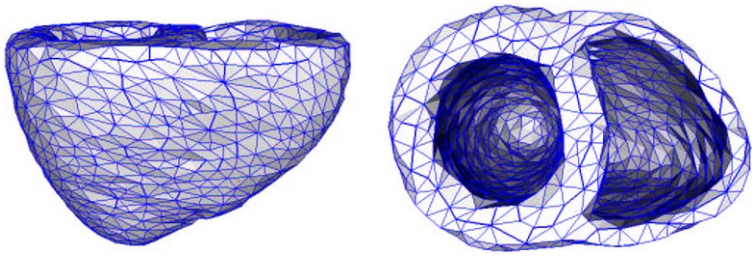

Fig. 9. Mesh of the heart.

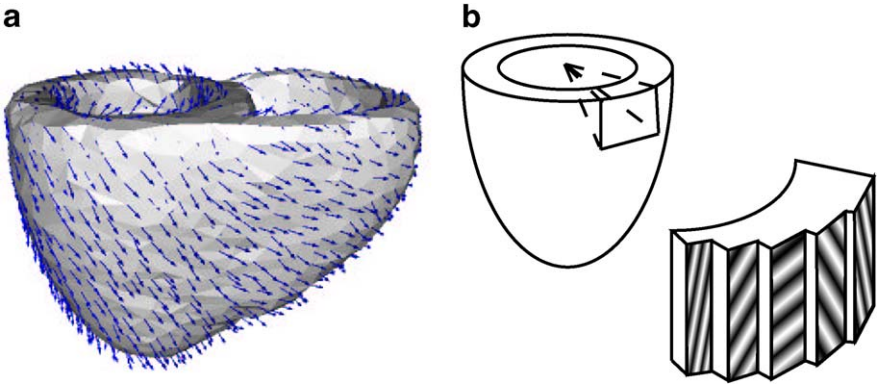

Fig. 10. Fibre orientations: (a) on the epicardium; (b) across the walls.

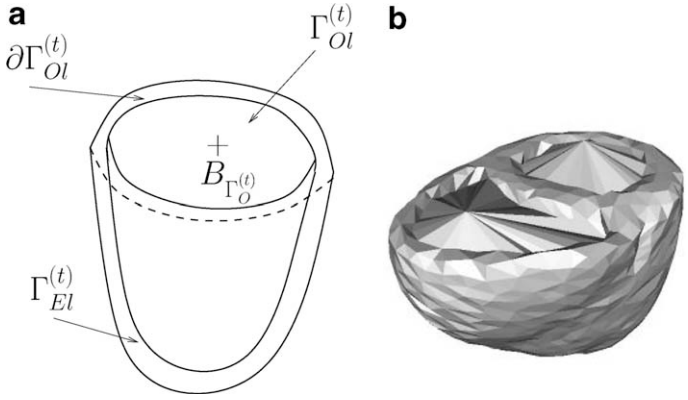

Fig. 11. (a) Left ventricle with surfaces $\Gamma_{Ol}^{(t)}$ and $\Gamma_{El}^{(t)}$; (b) the geometrical model including the closures $\Gamma_{Ol}^{(t)}$ and $\Gamma_{Or}^{(t)}$.

$$\int_{\Omega_H} \rho \ddot{\underline{y}}^{(t)} \cdot \underline{v} \,\mathrm{d}\Omega + \int_{\Omega_H} \underline{\underline{\Sigma}} : \delta\underline{\underline{E}} \,\mathrm{d}\Omega + \int_{\Gamma_{El} \cup \Gamma_{Er}} P_{\mathrm{v}}^{(t)} \underline{v} \cdot \underline{\underline{F}}^{-1} \cdot \underline{v} J \,\mathrm{d}\Gamma = 0 \quad \forall \underline{v} \in \mathscr{V}, \tag{24}$$

where $\mathscr{V}$ denotes a suitable space of displacement test functions and $\delta\underline{\underline{E}}$ the linearized strain variation corresponding to the virtual displacement $\underline{v}$, viz.

$$\delta E_{ij}(\underline{y}; \underline{v}) = \frac{1}{2}(v_{i,j} + v_{j,i} + \underline{y}_{,i} \cdot \underline{v}_{,j} + \underline{y}_{,j} \underline{v}_{,i}).$$

Note that P_{v} takes two different values in the two ventricles. In addition, according to (21) for each ventricle the outgoing flow is related to pressures by

$$\dot{V}^{(t)} = -f(P_{\mathrm{v}}^{(t)}, P_{\mathrm{ar}}^{(t)}, P_{\mathrm{at}}^{(t)}), \tag{25}$$

and intraventricular volumes are computed using the Ostrogradsky formula on the closed surface $\Gamma^{(t)} = \Gamma_E^{(t)} \cup \Gamma_O^{(t)}$ (see Fig. 11), transported to the corresponding reference surface Γ, viz.

$$V^{(t)} = \frac{1}{3} \int_{\Gamma^{(t)}} \underline{x} \cdot \underline{y}^{(t)} \,\mathrm{d}\Gamma^{(t)} = \frac{1}{3} \int_{\Gamma} \underline{y} \cdot \underline{\underline{F}}^{-1} \cdot \underline{x} J \,\mathrm{d}\Gamma, \tag{26}$$

where $\underline{x} = \underline{X} + \underline{y}$ are the updated position vectors.

Finally, the global problem we solve has – essentially – three unknowns:

- the displacement field $\underline{y}$;
- the field of contractile strains ε_c (an internal variable);
- the four-component vector $\mathbf{P}$ containing the values of the blood pressures in the ventricles and in the corresponding arterial outlets (the atrial pressures being considered as an input).

Accordingly, the major governing equations are the following:

- the equilibrium equation (24);
- the constitutive equation (15) which – together with (16) – relates the stress tensor to the strains $\underline{\underline{E}}$ and ε_c;
- the contraction law (1) which – together with the series balance equation (17) – provides a relation between $\underline{\underline{E}}$ and ε_c;
- the "valve laws" (25) – one equation for each ventricle – relating ventricular pressures and volumes with arterial (and prescribed atrial) pressures;
- the Windkessel models, see (22) and (23), relating ventricular volumes and arterial pressures – for the left and right ventricles separately.

3. Discretization of the heart model

In this section, we outline the numerical procedures used to discretize the heart model and to solve the resulting finite-dimensional problems.

3.1. Time and space discretization

The equilibrium equation (24) is time-discretized using the Newmark scheme, the stress $\underline{\underline{\Sigma}}$ given by (15) being discretized in the form

$$\underline{\underline{\Sigma}}^{\left(t+\frac{\Delta t}{2}\right)} = \underline{\underline{\Sigma}}\left(\underline{\underline{E}}^{\left(t+\frac{\Delta t}{2}\right)}, \dot{\underline{\underline{E}}}^{\left(t+\frac{\Delta t}{2}\right)}, \varepsilon_c^{\left(t+\frac{\Delta t}{2}\right)}, u^{\left(t+\frac{\Delta t}{2}\right)}\right).$$

All other equations describing state variables are discretized using a mid-point scheme i.e.

$$(\cdot)^{\left(t+\frac{\Delta t}{2}\right)} \approx [(\cdot)^{(t+\Delta t)} + (\cdot)^{(t)}]/2,$$
$$\dot{(\cdot)}^{\left(t+\frac{\Delta t}{2}\right)} \approx [(\cdot)^{(t+\Delta t)} - (\cdot)^{(t)}]/\Delta t.$$

In particular, the flow is related to the internal volume (hence to displacements) by

$$V^{(t+\Delta t)} - V^{(t)} + \frac{\Delta t}{2}(q^{(t+\Delta t)} + q^{(t)}) = 0. \tag{27}$$

Likewise, the mid-point scheme used for the Windkessel model given in (22) and (23) leads to equation

$$P_{\mathrm{ar}}^{(t+\Delta t)} - P_{\mathrm{ar}}^{(t)} + \frac{\Delta t}{C}\left[\frac{\frac{1}{2}(P_{\mathrm{ar}}^{(t+\Delta t)} + P_{\mathrm{ar}}^{(t)}) - P_{\mathrm{ve}}}{R_p} - \mathbb{I}_{P_{\mathrm{v}}^{\left(t+\frac{\Delta t}{2}\right)} \geqslant P_{\mathrm{ar}}^{\left(t+\frac{\Delta t}{2}\right)}} \times \left(\left(1 + \frac{R_c}{R_p}\right)\frac{q^{(t+\Delta t)} + q^{(t)}}{2} + \frac{CR_c}{\Delta t}\left(q^{(t+\Delta t)} - q^{(t)}\right)\right)\right] = 0, \tag{28}$$

where $\mathbb{I}_{P_v^{(t+\frac{\Delta t}{2})} \geqslant P_{ar}^{(t+\frac{\Delta t}{2})}}$ is 1 when $P_v^{(t+\frac{\Delta t}{2})} \geqslant P_{ar}^{(t+\frac{\Delta t}{2})}$ and 0 otherwise. At $t = t_0$ we assume a steady state (end of diastole), where $P_{ar} = 9310$ Pa and $q^{(0)} = 0$.

The numerical scheme allows to obtain explicit expressions of all state variables appearing in the contraction law (1) as functions of ε_c, namely, τ_c, k_c and σ_c at time step $t + \Delta t$ are expressed in terms of ε_c at time step $t + \Delta t$ and of the state variables at time step t. Therefore, the time discretization leads to a non-linear problem in $\underline{y}$, ε_c and $\mathbf{P}$ for each time step.

For the spatial discretization we use the finite element method [4] with Eq. (24), while ε_c is solved for each numerical integration point.

3.2. Solution of discrete problem

We thus obtain – for each time step – a non-linear system to be solved by a Newton-type procedure. The tangent linear system exhibits the following structure:

$$\begin{pmatrix} \mathbf{K_{11}} & \mathbf{K_{12}} & \mathbf{\Pi_1} \\ \mathbf{K_{21}} & \mathbf{K_{22}} & \mathbf{0} \\ \mathbf{\Pi_2} & \mathbf{0} & \mathbf{\Pi_3} \end{pmatrix} \begin{pmatrix} \mathbf{\Delta y} \\ \mathbf{\Delta \varepsilon_c} \\ \mathbf{\Delta P} \end{pmatrix} = \begin{pmatrix} \mathbf{f} \\ \mathbf{g} \\ \mathbf{h} \end{pmatrix}, \tag{29}$$

where the first row corresponds to (24), the second row to (1) combined with (17), and the third to the valve equation (25) together with the Windkessel equations.

In order to solve (29) we exploit the structure of $\mathbf{K_{22}}$ which is diagonal (since the equation in ε_c is written independently for each integration point), hence $\mathbf{\Delta \varepsilon_c}$ can be easily eliminated. Although $\mathbf{\Pi_3}$ can also be easily inverted, its Schur complement $\mathbf{\Pi_1 \Pi_3^{-1} \Pi_2}$ would change the pattern of non-zeros of $\mathbf{K_{11}}$, leading to time-demanding memory reallocations, hence we do not eliminate $\mathbf{\Delta P}$. Finally for each Newton iteration we solve

$$\begin{pmatrix} \mathbf{K_{11}} - \mathbf{K_{12}} \mathbf{K_{22}^{-1}} \mathbf{K_{21}} & \mathbf{\Pi_1} \\ \mathbf{\Pi_2} & \mathbf{\Pi_3} \end{pmatrix} \begin{pmatrix} \mathbf{\Delta y} \\ \mathbf{\Delta P} \end{pmatrix} = \begin{pmatrix} \mathbf{f} - \mathbf{K_{12}} \mathbf{K_{22}^{-1}} \mathbf{g} \\ \mathbf{h} \end{pmatrix}, \tag{30}$$

using a multifrontal sparse solver (UMFPACK package [12]), followed by

$$\mathbf{\Delta \varepsilon_c} = \mathbf{K_{22}^{-1}} (\mathbf{g} - \mathbf{K_{21}} \mathbf{\Delta y}). \tag{31}$$

4. Numerical simulations

In the results presented hereafter, the time step is taken constant with $\Delta t = 5$ ms. This value is largely determined by the isovolumetric phases durations (roughly 50 ms each). Considering the ejection and filling phases a larger time step could be used, hence an adaptative time step procedure could be introduced.

4.1. Calibration of the 3D model

A correct calibration of all the parameters used in the model is – of course – very important in order to obtain realistic simulations. The parameters to be calibrated can be divided into three groups:

- The parameters used in the arteries models can be estimated from data concerning pressure variations and phases lengths during a cardiac cycle. For more detailed considerations regarding the calibration of these parameters, see in particular [51,55] and the references therein.
- The main two parameters appearing in the contraction law (1) are k_0 and σ_0. The quantity σ_0 represents the asymptotic value for τ_c and can be estimated knowing the range of intraventricular blood pressure reached during muscle contraction. In our simulations we used $\sigma_0 = 300$ kPa and $k_0 = 150$ kPa.
- Concerning the calibration of the viscous and passive behaviors of the cardiac tissue, literature data are not as widely available as for soft tissues such as skin and tendons, see [54,44,18].

4.2. Simulation results

We now present some results of simulations carried out with the complete heart model previously described. For animated versions of these results see [49].

These results have been obtained after a simulation of several cardiac cycles so that the approximate initial conditions are of no significance. Indeed, the stability of the model is demonstrated by results obtained over a sequence of cycles, which shows that the system rapidly reaches an attractor (limit cycle), whether after initialization or following a modification of the parameters, see Fig. 12.

Fig. 13 shows some classical indicators characteristic of the cardiac function. The quantities displayed are (from left to right and from top to bottom): left ventricle volume variations, blood pressure variations (with P_{lv}, P_{ao} and P_{at} denoting the pressures in the left ventricle, aorta and left atrium, respectively), aortic flow and mitral flow, mitral annulus displacement along the apex–base axis, contractile

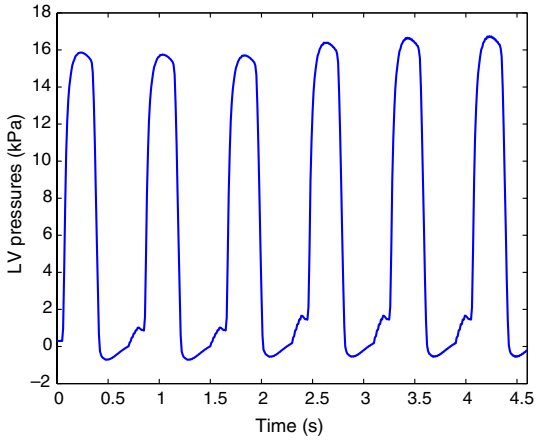

Fig. 12. Blood pressure P_v in the left ventricle over six cycles; a modification of P_{at} in the left compartment is introduced before the fourth cycle.

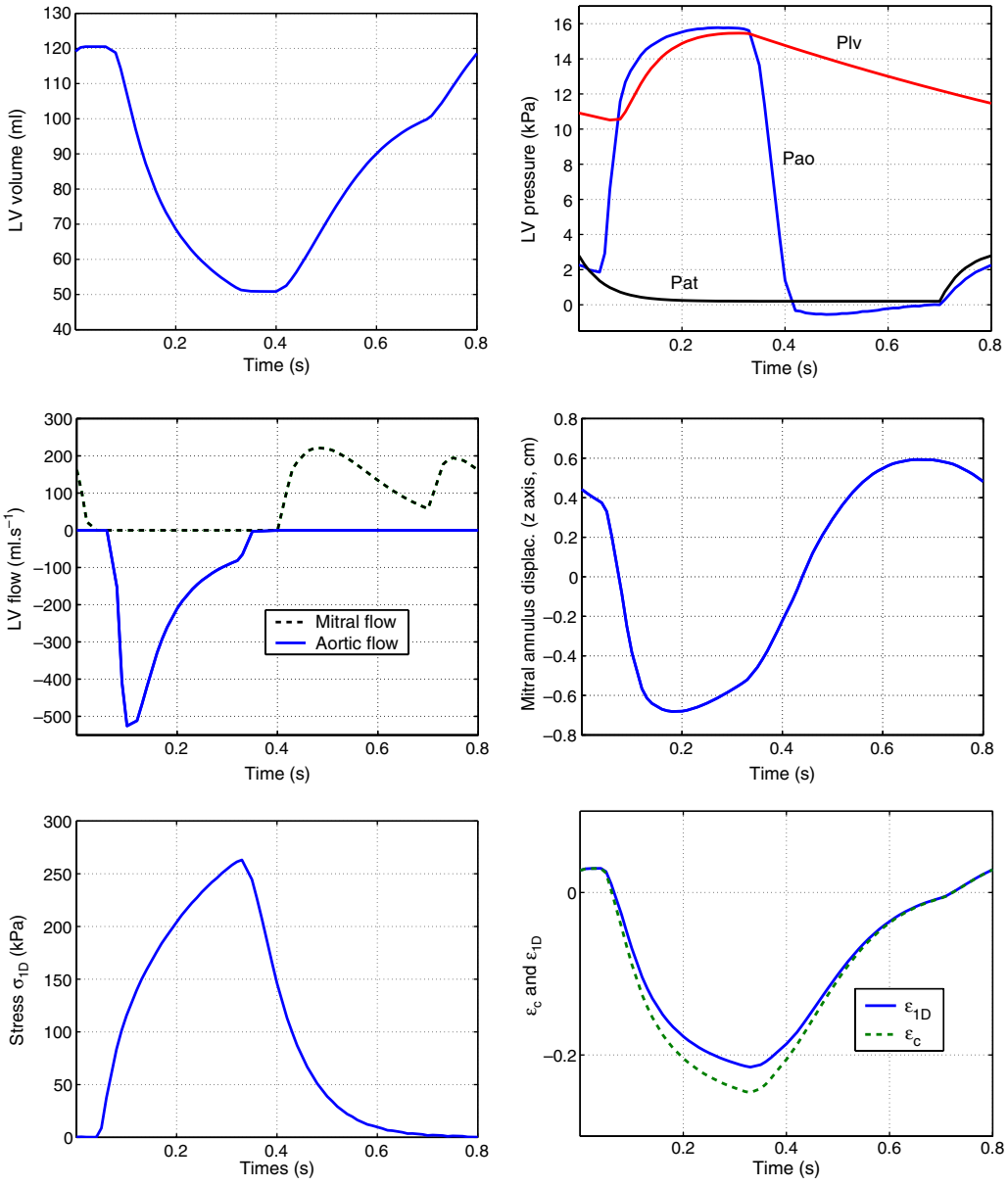

Fig. 13. Global indicators of the cardiac function for the left ventricle.

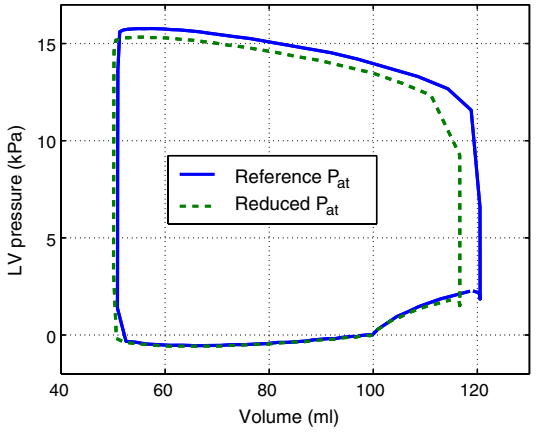

Fig. 14. P–V cycle for two different mitral pressures (Starling effect).

stress, strains in the fibre direction for a given point of the myocardium. Fig. 14 illustrates the Starling effect. Namely, two P–V cycles for the left ventricle, obtained with two different mitral pressures are plotted demonstrating how the stroke volume increases with the mitral pressure.

We also point out that – since we do not use a mixed displacement–pressure formulation – we only obtain approximate incompressibility of the cardiac tissue by penalizing the volume variations, see Section 2.3.4. Fig. 15 shows the typical volume variations for a sample of tetrahedra during a cardiac cycle.

We finally present simulation results representing a pathological case. As a simplified model of an infarcted heart, we considered reduced values of the contraction parameters k_0 and σ_0 in two given areas corresponding to regions of interest specified by the American Heart Associ-

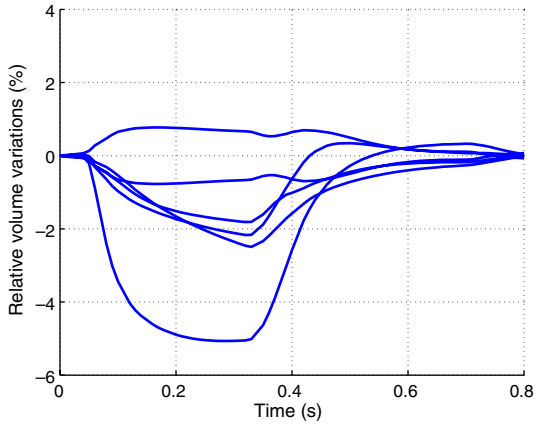

Fig. 15. Volume variations along a cardiac cycles for a sample of tetrahedra.

Fig. 16. Areas with reduced contractility: $\sigma_0 = 100$, 200 kPa, instead of the reference value $\sigma_0 = 350$ kPa ($k_0 = \sigma_0/2$ in all areas).

ation, see Fig. 16. The strains at the end of the ejection are shown in Fig. 17. We note that the tissue stretches – instead of contracting – within the affected areas, as expected. The global indicators of the cardiac function for the pathological case are presented and compared with the reference case in Fig. 18. We observe that the ejected volume and maximum ventricular pressure are significantly reduced in the impaired organ.

5. Data assimilation for the heart

In this section we further discuss the objectives and challenges of data assimilation in association with heart modeling, and we present some preliminary results obtained in this direction.

5.1. The aim of data assimilation

The aim of data assimilation is to incorporate measurements into the model of a dynamical system in order to obtain accurate estimates of the past, current – and possibly future – state variables, parameters, initial conditions and input of the model.

Data assimilation is particularly valuable when the various quantities (parameters, initial conditions, inputs,...) that need be prescribed in order to solve the model equations cannot be fully determined *a priori*. A data assimilation procedure is designed to combine actual measurements with model simulations in order to estimate these quantities jointly with the state variables of the model. Data assimilation is – for example – widely used in meteorology and oceanography, in order to process the abundant measurements received in real time from a variety of sensors (e.g., satellites, aircraft, ships and land stations).

The various forms of data assimilation methodologies use ideas originating from different branches of mathematics, and in particular from probabilities, optimization and control theory. These methodologies can be divided into two main categories, namely, the variational and sequential approaches which we now summarize. Denoting by H the observation operator, $\{Y_{t_k}\}_{k\in I}$ the available measurements and X_t the model response, data assimilation seeks the minimization of a cost function such as

$$J = \frac{1}{2}\sum_{k\in I} \|Y_{t_k} - HX_{t_k}\|^2_{\Omega_H}.$$

Minimization is performed over the set of quantities to be estimated: state variables constrained to satisfy the model equations, parameters,... The symbol $\|.\|_{\Omega_H}$ denotes a suitable norm associated with the problem formulation and $t_k \in \mathcal{J}$ for all $k \in I$. Note that the cost function written here in a discrete time framework could also be expressed as an integral in continuous time. If the set of time steps $\mathcal{J}$ covers the complete simulation time interval $[t_0, T]$, the assimilation technique is said to be *variational* and corresponds to an optimal control problem, see e.g. [11,31,34,52]. By contrast if at each time step t_k, $\mathcal{J} = [t_0, t_k]$, then the assimilation procedure is said to be *sequential* and corresponds in general to a filtering technique. This approach has been introduced by Kalman in the 1960s [25,26] and is widely used in various domains [8,27,30].

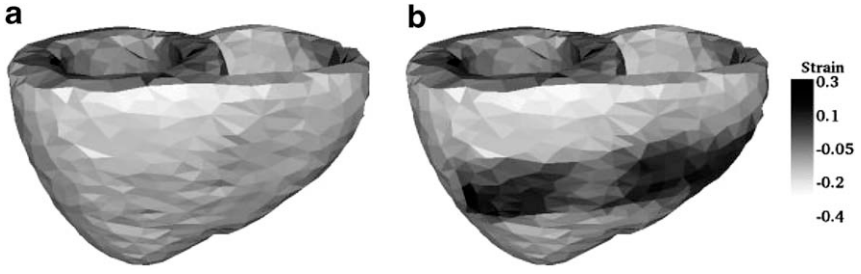

Fig. 17. Strain ε_{1D} (end systole), (a) reference situation and (b) pathological case.

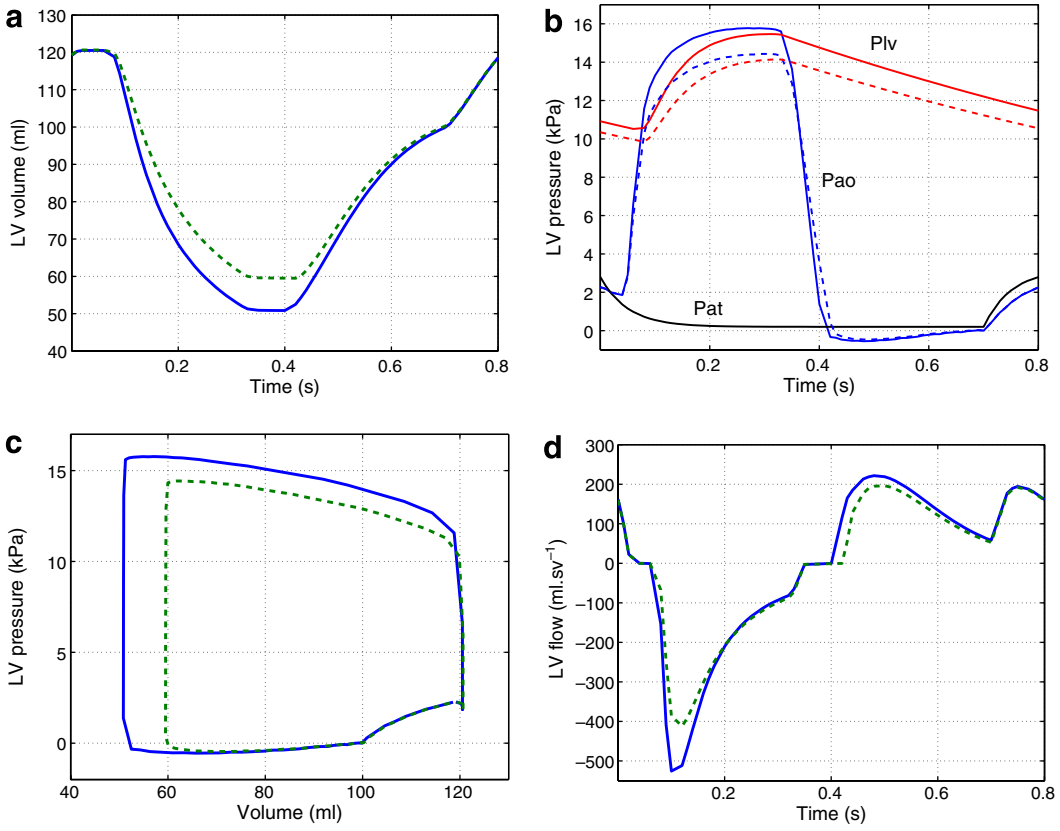

Fig. 18. Global indicators of cardiac function (solid line: reference case, dashed line: pathologic case). For the left ventricle, (a) volume variations, (b) pressions variations (c) PV loop, (d) LV inflow (>0) and outflow (<0).

As regards the heart behavior, although data acquisition techniques (ECG, ultrasound or MRI images,...) have greatly improved during the last decades and are very valuable for clinical purposes [41], the available measurements are still relatively scarce and noisy. In addition, some crucial biological quantities are hardly – or not at all – accessible in the data, as e.g. for stresses and pressures. Also, of course, *a priori* experimenting cannot be used to determine accurate values of constitutive parameters for the heart of a given patient and – indeed – the estimation of some such parameters can be of utmost clinical value for diagnosis purposes, for example to determine the extent and localization of an infarct. Therefore, resorting to data assimilation is particularly attractive in this context, and we now report on some preliminary results obtained within this perspective.

5.2. Data assimilation procedure and results

Of course, due to the complexity of the model and to observability considerations it is not possible to estimate all the quantities entering the model equations.

We emphasize that, with the proposed model, many different cardiac pathologies can be potentially characterized by varying – for each pathology – a limited number of parameters only. In the sequel, we focus on the estimation of parameters that are of particular clinical interest in the case of ischemia or post-infarct situations, namely, the contractility coefficient σ_0 featured in (1).

Classical sequential data assimilation techniques leading to prohibitive computing costs, we consider the variational approach. Thus, since σ_0 is to be estimated, we want to solve the problem

$$\sigma_0^{\text{aim}} = \operatorname{argmin}\left\{J(\sigma_0)|\sigma_0 = \{\sigma_{0_j}\}_{j=1}^{n} \in \mathscr{R}^n\right\} \tag{32}$$

with constraints

$$\begin{aligned} &\Phi^{(t_i)}(X_{t_i}, X_{t_{i-1}}, \sigma_0) = 0, \quad i = 1, \ldots, N, \\ &\sigma_{0_j}^{\min} < \sigma_{0_j} < \sigma_{0_j}^{\max} \quad \text{for } j = 1, \ldots, n, \end{aligned} \tag{33}$$

where $\Phi^{(t_i)}(X_{t_i}, X_{t_{i-1}}, \sigma_0) = 0$ represents the 3D model discretized in space and time. In (32), n denotes the number of unknown in σ_0 i.e. the number of areas in the myocardium associated with unknown values of the contractility σ_0. The extended state vector X in our case is

$$X := [y \quad \varepsilon_c \quad \mathbf{P}]^{\mathrm{T}}.$$

Note that time instants with index i correspond to the discretized time for the simulation whereas time instants with index k correspond to the instants for which a measurement is available. The gradient of J is

$$\nabla_{\sigma_0} J = -\sum_{k \in I} \left\langle Y_{t_k} - HX_{t_k}, H\frac{\partial X_{t_k}}{\partial \sigma_0} \right\rangle, \tag{34}$$

where $\frac{\partial X_{t_k}}{\partial \sigma_0}$ can be obtained by differentiating (33), which gives

$$\begin{aligned} &\frac{\partial \Phi^{(t_i)}}{\partial \sigma_0} + \frac{\partial \Phi^{(t_i)}}{\partial X_{t_i}} \frac{\partial X_{t_i}}{\partial \sigma_0} + \frac{\partial \Phi^{(t_i)}}{\partial X_{t_{i-1}}} \frac{\partial X_{t_{i-1}}}{\partial \sigma_0} = 0, \quad i = 1, \ldots, N, \\ &\frac{\partial X_0}{\partial \sigma_0} = 0, \end{aligned} \tag{35}$$

see also [46,47] for a similar approach. Denoting $\Phi_{\sigma}^{(t_i)} \equiv \frac{\partial \Phi^{(t_i)}}{\partial \sigma_0}$, $\Phi_X^{(t_i)} \equiv \frac{\partial \Phi^{(t_i)}}{\partial X_{t_i}}$, $\Phi_{Xp}^{(t_i)} \equiv \frac{\partial \Phi^{(t_i)}}{\partial X_{t_{i-1}}}$ and $S_{t_i} \equiv \frac{\partial X_{t_i}}{\partial \sigma_0}$, we can write:

$$S^{(0)} = 0$$

$$\Phi_X^{(t_i)} S_{t_i} = -(\Phi_{\sigma}^{(t_i)} + \Phi_{Xp}^{(t_i)} S^{(t_{i-1})}), \quad i = 1, \ldots, N.$$

An outline of the data assimilation algorithm is as follows:

- for time steps $i = 1, \ldots, N$:
  - solve state problem $\Phi^{(t_i)}(\sigma_0, X_{t_i}, X_{t_{i-1}}) = 0$,
  - from $\Phi_X^{(t_i)} S_{t_i} = -(\Phi_{\sigma}^{(t_i)} + \Phi_{Xp}^{(t_i)} S^{(t_{i-1})})$ obtain S_{t_i},
  - compute $\nabla_{\sigma_0} J$ from Eq. (34),
- employ $\nabla_{\sigma_0} J$ in a gradient method (we use the reflective Gauss–Newton method available with Matlab) to update $\sigma_0 = \{\sigma_{0_j}\}_{j=1}^{n}$ until the gradient is sufficiently small.

  The results that we now present have been obtained using numerically simulated measurements assimilated with the complete 3D problem. More specifically, the test problem considered is constructed in the following manner.
- The 3D problem is simulated with given parameters $\sigma_0 = \{\sigma_{0_j}\}_{j=1}^{3}$ as considered in Section 4.2, see Fig. 16. The measurements $\{Y_{M_p,t_k}\}_{p,k}$ are generated using

  $$Y_{M_p,t_k} = HX_{M_p,t_k} + v(M_p, t_k),$$

  H being the chosen observation operator and v a noise in the measurements. Each $v(M_p, t_k)$ is chosen from a uniform distribution on the interval $0.05\max_{p,k}(|HX_{M_p,t_k}|) * [-1, 1]$. Here we consider only displacements for 20 points $\{M_p\}_{p=1}^{20}$ randomly located at the epicardium and endocardium of the muscle and recorded at time steps $t_k = t_0 + 3k\Delta t$, $\Delta t = 5$ ms.

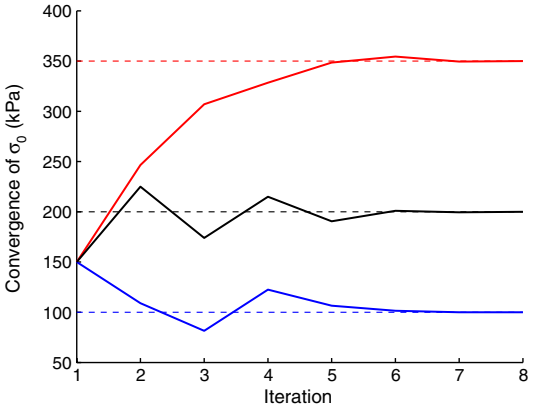

Fig. 19. Convergence of σ_{0_j} along iterations of the data assimilation, (--) reference value and (—) estimated value.

- Starting from given parameters $\hat{\sigma}_0 = \{\hat{\sigma}_{0_j}\}_{j=1}^{3}$ different from the original values, the data assimilation is carried out. The objective is to obtain $\hat{\sigma}_0 \approx \sigma_0$.

The variations of the 3 values of σ_0 along the identification steps are illustrated in Fig. 19 where it appears that an accurate estimation of the parameters $\{\sigma_{0_j}\}_{j=1}^{3}$ characterizing the impact of an infarct is obtained after six iterations.

6. Conclusions

We have proposed an electrically activated 3D mechanical model of the heart muscle. The modeling, the numerical implementation and the simulations were presented in this article. The main conclusion is that, even if more complete validations have to be carried out, our model seems to be able to reproduce some behaviors of a pathological or healthy heart as measured in clinical data. We have also presented preliminary results concerning data assimilation techniques in order to detect contraction troubles.

We are currently pursuing and extending this work in the following directions:

- complete validation and calibration of the model,
- mathematical analysis of the model,
- data assimilation in 3D with real data, see [48],
- modeling of blood perfusion in the muscle, see [9].

Another perspective is to estimate APD (action potential duration) and DT (depolarization time) from measurements of the mechanical activity synchronized by standard ECG. If this could be achieved, a complete estimation of the electrical traveling wave, useful to detect conductivity trouble, would be possible from the mechanical response of the system.

One of the major difficulties to be confronted in this approach lies in the conflict between the complexity of the model to be used (number of quantities to estimate) and the features (scarcity, quantities measured,...) of the measurements available in a clinical environment. Current techniques provide data on the electrical activity and the ventricular wall displacements. Even if the identification results presented here only used displacements measurements, in practice complementary data pertaining to stresses in the muscle or blood pressures – especially during isovolumetric phases – may be needed.

Acknowledgements

This work has been carried out in the framework of the multidisciplinary research projects ICEMA (Images of the Cardiac ElectroMechanical Activity, see [3,40]) and CardioSense3D [6] involving several teams from academic institutions and industrial partners. The work of the third

author was supported by the Ministry of Education of the Czech Republic (Research Project MSM 4977751303).

References

[1] Aliev R, Panfilov AV. A simple two-variable model of cardiac excitation. Chaos, Solitons Fractals 1996;7:293–301.

[2] Avolio AP. Multi-branched model of the human arterial system. Med Biol Eng Comput 1980;18(6):709–18.

[3] Ayache N, Chapelle D, Clément F, Coudière Y, Delingette H, Désidéri JA, et al. Towards model-based estimation of the cardiac electro-mechanical activity from ECG signals and ultrasound images. In: Katila T, Magnin IE, Clarysse P, Montagnat J, Nenonen J, editors. Lectures notes in computer science, vol. 2230. Springer-Verlag; 2001.

[4] Bathe KJ. Finite element procedures. Prentice Hall; 1996.

[5] Bestel J, Clément F, Sorine M. A biomechanical model of muscle contraction. In: Niessen WJ, Viergever MA, editors. Lectures notes in computer science, vol. 2208. Springer-Verlag; 2001.

[6] CardioSense3D. Available from: http://www-sop.inria.fr/CardioSense3D/.

[7] Chapelle D, Clément F, Génot F, Le Tallec P, Sorine M, Urquiza J. A physiologically-based model for the active cardiac muscle. In: Katila T, Magnin IE, Clarysse P, Montagnat J, Nenonen J, editors. Lectures notes in computer science, vol. 2230. Springer-Verlag; 2001.

[8] Chui CK, Chen G. Kalman filtering with real time applications. Springer-Verlag; 1999.

[9] Cimrman R, Rohan E. Modelling heart tissue using a composite muscle model with blood perfusion. In: Bathe KJ, editor. Second M.I.T. conference on computational fluid and solid mechanics. Massachusetts Institute of Technology; 2003. p. 1642–6.

[10] Costa KD, Holmes JW, McCulloch AD. Modeling cardiac mechanical properties in three dimensions. Phil Trans R Soc Lond A 2001; 359:1233–50.

[11] Courtier P, Talagrand O. Variational assimilation of meteorological observations with the adjoint vorticity equation Part 2: Numerical results. Quart J Roy Meteorol Soc 1987;113:1329–47.

[12] Davis TA. Algorithm 8xx: UMFPACK V4.1, an unsymmetric-pattern multifrontal method with a column pre-ordering strategy. Technical report, University of Florida, CISE Department, 2003. Also TR-03-007 at www.cise.ufl.edu/tech-reports.

[13] Djabella K, Sorine M. Differential model of excitation–contraction coupling in a cardiac cell for multicycle simulations. In: 3rd European medical and biological engineering conference, Prague, 2005.

[14] Formaggia L, Lamponi D, Quarteroni A. One-dimensional models for blood flow in arteries. J Eng Math 2003;47(3–4):251–76.

[15] Fung YC. Biomechanics: mechanical properties of living tissues. second ed. Springer-Verlag; 1993.

[16] Hill AV. The heat of shortening and the dynamic constants in muscle. Proc Roy Soc Lond (B) 1938;126:136–95.

[17] Hsu E, Henriquez C. Myocardial fiber orientation mapping using reduced encoding diffusion tensor imaging. J Cardiovasc Magn Reson 2001;3.

[18] Humphrey JD. Continuum biomechanics of soft tissues. Proc R Soc Lond A 2002;459:3–46.

[19] Hunter PJ, McCulloch AD, ter Keurs HED. Modelling the mechanical properties of cardiac muscle. Prog Biophys Mol Biol 1998;69:289–331.

[20] Hunter PJ, Kohl P, Noble D. Integrative models of the heart: achievements and limitations. Phil Trans R Soc Lond A 2001;359(1783):1049–54.

[21] Hunter PJ, Nash MP, Sands GB. Computational electromechanics of the heart. In: Panfilov AV, Holden AV, editors. Computational biology of the heart. John Wiley & Sons; 1997. p. 345–407.

[22] Hunter PJ, Pullan AJ, Smaill BH. Modeling total heart function. In: Yarmush ML, Diller KR, Toner M, editors. Annual review of biomedical engineering, vol. 5. North-Holland; 2003. p. 465–622.

[23] Huxley AF. Muscle structure and theories of contraction. Progress in biophysics and biological chemistry, vol. 7. Pergamon Press; 1957. p. 255–318.

[24] Jülicher F, Ajdari A, Prost J. Modeling molecular motors. Rev Mod Phys 1997;69(4).

[25] Kalman RE. A new approach to linear filtering and prediction problems. ASME Trans – J Basic Eng 1960;82(Series D):35–45.

[26] Kalman RE, Bucy RS. New results in linear filtering and prediction theory. ASME Trans – J Basic Eng 1961;83(Series D):95–108.

[27] Kano H, Ghosh BK, Kanai H. Single camera based motion and shape estimation using extended Kalman filtering. Math Comput Modell 2001;34(5–6):511–25.

[28] Kauer M. Inverse finite element characterization of soft tissues with aspiration. PhD thesis, Swiss Federal Institute of Technology, 2001.

[29] Keener JP, Sneyd J. Mathematical physiology. New York: Springer-Verlag; 1998.

[30] Kellerhals BP. Financial pricing models in continuous time and Kalman filtering. Lecture Notes Econ Math Syst 2001;506.

[31] Le Dimet FX, Talagrand O. Variational algorithms for analysis and assimilation of meteorological observation: theoretical aspects. Tellus 1986;38:97–110.

[32] Le Tallec P. In: Ciarlet PG, Lions JL, editors. Numerical methods for nonlinear three-dimensional elasticity. Handbook of numerical analysis, vol. 3. North-Holland; 1994. p. 465–622.

[33] Lin DH, Yin FC. A multiaxial constitutive law for mammalian left ventricular myocardium in steady-state barium contracture or tetanus. J Biomech Eng 1998;120(4):504–17.

[34] Lions JL. Contrôle optimal des systèmes gouvernés par des équations aux dérivées partielles. Dunod; 1968.

[35] MacDonald DA. Blood flow in arteries. Edward Harold Press; 1974.

[36] Mercier J, DiSessa T, Jarmakani J, Nakanishi T, Hiraishi S, Isabel-Jones J, et al. Two-dimensional echocardiographic assessment of left ventricular volumes and ejection fraction in children. Circulation 1982;65.

[37] Mirsky I, Parmley WW. Assessment of passive elastic stiffness for isolated heart muscle and the intact heart. Circul Res 1973;33:233–43.

[38] Monti A, Médigue C, Sorine M. Short-term modelling of the controlled cardiovascular system. ESAIM Proc 2002;12:115–28.

[39] Mulquiney PJ, Smith NP, Clark K, Hunter PJ. Mathematical modelling of the ischaemic heart. Nonlinear Anal 2001;47:235–44.

[40] ICEMA (Images of Cardiac Electro-Mechanical Activity). Available from: http://www-rocq.inria.fr/sosso/icema2/icema2.html.

[41] Frangi AF, Radeva PI, Santos A, Hernandez M, editors. Proceedings of the third international workshop functional imaging and modeling of the heart, FIMH2005. Lecture notes in computer science, vol. 3504, 2005.

[42] Pennacchio M, Colli Franzone P, Guerri L, Taccardi B. A bidomain explanation of the multiple waveforms in electrograms. In XXVII International Congress on Electrocardiology, Rome, 2000.

[43] Peskin CS. The immersed boundary method. Acta Num 2002;11: 479–517.

[44] Pioletti DP, Rakotomanana LR. Non linear viscoelastic laws for soft biological tissues. Eur J Mech A/Solids 2000;19:749–59.

[45] Pioletti DP, Rakotomanana LR, Benvenuti JF, Leyvraz PF. Viscoelastic constitutive law in large deformations: application to human knee ligaments and tendons. J Biomech 1998;31:753–7.

[46] Rohan E, Cimrman R. Sensitivity analysis and material identification for activated smooth muscle. Comput Assist Mech Eng Sci 2002;9: 519–41.

[47] Rohan E, Whiteman JR. Shape optimization of elasto-plastic structures and continua. Comput Methods Appl Mech Eng 2000;187:261–88.

[48] Sermesant M, Moireau P, Camara O, Sainte-Marie J, Andriantsimiavona R, Cimrman R, et al., Cardiac function estimation from MRI using a heart model and data assimilation: advances and difficulties. In: Frangi AF, Radeva PI, Santos A, Hernandez M, editors. Proceedings of the third international workshop functional imaging and modeling of the heart, LNCS, vol. 3504, 2005.

[49] Web site of the MACS team. Available from: http://www-rocq.inria.fr/MACS/Coeur/index.html.
[50] Smaill BH, Hunter PJ. Structure and function of the diastolic heart: material properties of passive myocardium. Theory of heart: biomechanics, biophysics, and nonlinear dynamics of cardiac function. New York: Springer-Verlag; 1991.
[51] Stergiopulos N, Westerhof BE, Westerhof N. Total arterial inertance as the fourth element of the windkessel model. Am J Physiol 1999;276:H81–8.
[52] Talagrand O, Courtier P. Variational assimilation of meteorological observations with the adjoint vorticity equation Part 1: Theory. Quart J Roy Meteorol Soc 1987;113:1311–28.
[53] Truesdell C, Noll W. The non-linear field theories of mechanics. second ed. Berlin: Springer; 1992.
[54] Veronda DR, Westmann RA. Mechanical characterization of skin-finite deformation. J Biomech 1970;3:114–24.
[55] Westerhof N, Bosman F, De Vries CJ, Noordegraaf A. Analog study of the human systemic arterial tree. J Biomech 1969;2:121–43.
[56] Wu JZ, Herzog W. Modelling concentric contraction of muscle using an improved cross-bridge model. J Biomechan 1999;32:837–48.
[57] Zahalak GI. A distribution moment approximation for kinetic theories of muscular contraction. Math Biosci 1981;55:89–114.